

Majid Asli, Panagiotis Stathopoulos

An optimization methodology for turbines driven by pulsed detonation combustors

Open Access via institutional repository of Technische Universität Berlin

Document type

Journal article | Accepted version

(i. e. final author-created version that incorporates referee comments and is the version accepted for publication; also known as: Author's Accepted Manuscript (AAM), Final Draft, Postprint)

This version is available at

<https://doi.org/10.14279/depositonce-16405>

Citation details

Asli, M., & Stathopoulos, P. (2022). An Optimization Methodology for Turbines Driven by Pulsed Detonation Combustors. In Journal of Engineering for Gas Turbines and Power. ASME International.
<https://doi.org/10.1115/1.4055490>.

Terms of use

© This work is licensed under a Creative Commons Attribution 4.0 International license:
<https://creativecommons.org/licenses/by/4.0/>

An optimization methodology for turbines driven by pulsed detonation combustors

Majid Asli*

Chair of Fluid Dynamics,
Technical University of Berlin
Berlin, 10623, Germany
Email: asli@campus.tu-berlin.de

Panagiotis Stathopoulos

Institute of Low-Carbon
Industrial Processes
German Aerospace Center (DLR)
Cottbus, Germany
Email: Panagiotis.Stathopoulos@dlr.de

ABSTRACT

A step-change in efficiency of gas turbine technology and, subsequently, an emissions reduction from this technology requires conceptual changes. Substituting conventional combustion chambers with pressure gain combustion in the form of pulsed detonation combustion (PDC) is one of the promising methods that can reduce gas turbine emissions significantly. Nevertheless, the component matching for the respective systems and specifically that of turbine expanders working with the exhaust flow of PDC tubes is still not solved. The unsteady nature of PDC exhaust flow makes 3D-CFD simulations too expensive to be applied in optimization loops in early design stages. To address this question, the present paper introduces a new cost-effective but reliable methodology for turbine analysis and optimization, based on the unsteady exhaust flow of pulsed detonation combustors. The methodology unitizes a robust unsteady one-dimensional solver, a meanline performance analysis, and an adaptive surrogate optimization algorithm. A two-stage axial

*Corresponding author.
GTP-22-1330

turbine is optimized considering all unsteady flow features of a hydrogen-air PDC configuration with five PDC tubes. A three-dimensional URANS simulation is performed for the optimized geometry and the baseline to evaluate the methodology. The results showed that the optimized turbine produces 16% lower entropy than the original one. Additionally, the turbine output power is increased by 14% by the optimized design. Based on the results, it is concluded that the approach is fast and reliable enough to be applied in optimizing any turbine working with unsteady flows, more specifically in PDC applications.

NOMENCLATURE

A Cross sectional area.

E Internal energy.

F Force.

F_e Endwall force.

f Frequency.

H Total enthalpy.

h Specific enthalpy.

\dot{m} Mass flow rate.

NB Number of blade.

n Number of sample points.

P Pressure, static pressure.

Pr Pressure ratio.

rpm Round per minute.

S Non-dimensional entropy.

\bar{S} Time averaged non-dimensional entropy.

T Temperature.

t Time.

$t_{r,max}/c$ Thickness to chord ratio for the first rotor blade.

V Flow velocity.

W Work.

X Sample point in a design space.

Y Mass fraction.

y^+ Dimensionless wall distance.

β Blade outlet angle.

ρ Density.

γ Heat capacity ratio.

ω Total pressure loss coefficient.

Abbreviations

CSM Complex Shape Method.

E^3 Energy Efficient Engine.

GCI Grid Convergence Index.

LHD Latin Hypercube Design.

PDC Pulsed Detonation Combustion.

PGC Pressure Gain Combustion.

RDC Rotating Detonation Combustion.

SBO Surrogate Based Optimization.

URANS Unsteady Reynolds-Averaged Navier Stocks.

Subscript

b Best sample point.

bl Bleed flow.

$Cont$ Contraction.

Exp Expansion.

o Sample point that is neither the best nor the worst.

R Rotor number 1.

Ref Reflection.

ref Reference value.

s Geometric center of the complex shape.

sp Species.

t Total quantity.

V Nozzle number 1.

w Worst sample point.

x Axial direction.

Superscript

(*j*) Complex shape j^{th} .

INTRODUCTION

The power generation and transport sectors have been responsible for most of the global growth of greenhouse gas emissions for the last decade. They also accounted for over two-thirds of emissions in 2019 [1]. This is only a piece of statistics indicating that achieving net-zero economies by 2050 very much depends on measures in areas other than the energy sector. Gas turbines can be considered the heart of energy and aviation sectors that need to be modified for this purpose.

Among the solutions for significantly cutting gas turbine emissions, using pressure gain combustion (PGC) instead of constant pressure combustion has shown its potential [2]. Despite the higher thermal efficiency of PGC-driven gas turbine cycles, which have been proven theoretically [3, 4], almost all practical PGC processes include unsteady physical phenomena. The associated unsteady exhausting flow results in an operation of turbomachinery components under fluctuating off-design conditions. In turn, this causes a reduction in their performance and can counteract all benefits from the introduction of PGC. In order to make the PGC-gas turbine concept practical, efficient turbomachinery components capable of working in a wide range of operating conditions are required. Several researchers have focused on integrating turbines into the PGC concepts of pulsed detonation combustion (PDC) and rotating detonation combustion (RDC). In most experimental studies, existing turbines are placed downstream of PGCs to evaluate their performance. Glaser et al. [5] quantified a turbine's performance connected to a circular array of six PDC tubes by measuring the turbine power. They showed a comparable turbine efficiency

between PDC-driven and steady operating turbines across the tested pressure ratios. They also concluded that an increase in fill fraction leads to a reduction in turbine efficiency. Rasheed et al. [6] connected six PDC tubes to a single-stage axial turbine and measured the work extraction and peak pressure attenuation through the blade rows. They also concluded the necessity of design optimization for a turbine working with PDCs [7]. Anand et al. [8] measured a higher thermal efficiency for the PDC cycle than the theoretical Brayton cycle, despite a substantial reduction in turbine efficiency. Fernelius and Gorrell [9] utilized a rotating ball valve to generate a sinusoidal pressure pulse to mitigate PDC exhaust flow for a combustion-free turbine test rig. They observed a decrease in turbine efficiency and pressure ratio and concluded that the cause is the pressure pulse amplitude, not the frequency.

While the highly unsteady exhaust flow of PDC and the compact geometry bring measurement challenges, numerical methods can provide more details, specifically where it is not possible to observe experimentally. A three-dimensional simulation of a PDC tube connected to an aircraft engine axial turbine stage was done by Van Zante et al. [10] to evaluate the pressure attenuation through the turbine stage. They measured a very low turbine efficiency of 26.7% since it operated for a significant part of the PDC cycle at off-design conditions. Xisto et al. [11] performed a two-dimensional URANS simulation of a coupled PDC-turbine system to study the different loss sources in turbines. They observed that the mismatch between the rotor speed and time-varying exhaust flow of PDC tubes is responsible for large incidence angle variation and, consequently, flow separation and significant losses. Their numerical simulation has shown that the turbine operates more efficiently under purge conditions for the particular turbine design. Cuciumita and Paschereit [12] compared the performance of a supersonic turbine stage under steady inlet and unsteady flow of PDC tubes using a two-dimensional RANS solver. They computed a pressure loss that was 50% smaller in the case of PDC operated turbine, which was mainly due to the turbine being exposed to the shock waves for less time.

Despite the accuracy of unsteady two and three-dimensional CFD methods in capturing detailed flow physics, their computational price does not allow these methods to be utilized in optimization loops, where many simulations have to be performed. Instead, low fidelity methods are

required to carry out design and optimization simulations fast and reliably. Within the scope of turbine and PDC optimization, Fernelius and Gorrell [13] utilized a two-dimensional steady RANS solver to calculate the objective function and optimize the rotor blades of a turbine stage. To simplify the optimization problem, they assumed a sinusoidal pressure pulse as the turbine inlet boundary condition. They performed steady simulations, one at a maximum and one at a minimum of the pressure pulse in each objective function call. However, the unsteady features of the PDC exhaust flow field were ignored for the sake of reducing computational time. While the mean line methods in turbomachinery are steady solvers, one-dimensional methods can be used in unsteady cases [14–16]. Chiong et al. [17] proposed integration of a 1D-Euler solver with a meanline analysis for a mixed-flow turbocharger turbine. They used the meanline method for every discrete point on the inflow pulse to calculate the tangential velocity to the rotor. Recently, the authors have developed a 1D-Euler methodology for simulating turbines working under PDC exhaust flows [18]. We have shown the approach's applicability with an acceptable level of accuracy.

According to the literature, no systematic procedure has been introduced providing a turbine optimization method that considers the PDC unsteady flow features inside the optimization loops. The present paper aims to fill this gap by presenting an optimization procedure based on a surrogate model using a time-dependent one-dimensional Euler solver to evaluate the objective function. The solver uses mean line performance analysis to provide source terms in the governing equations. A PDC model provides the unsteady turbine simulations with the inlet boundary conditions. The test case is a two-stage high-pressure turbine connected to a five-tube PDC array and a plenum in between. To evaluate the methodology, three-dimensional URANS simulations will be utilized to compare the optimum design against the baseline.

METHODS

The paper focuses on introducing of an optimization procedure in the initial design procedure of a turbine for PDC. This includes methodologies to calculate the objective function and its prerequisites, optimization algorithm, and verification method. In this section, firstly, the test case is described. This is followed by the discussion of a coupled combustion model for calculating PDC

exhaust flow condition, a 1D-Euler solver for evaluating the objective function, and the optimization algorithm. Finally, the unsteady 3D-CFD simulation will be explained and applied for the optimized and baseline geometries under the same boundary conditions.

Turbine Model

The baseline design for the current work is the high-pressure turbine of the Energy Efficient Engine project reported by NASA [19]. The turbine has two stages of moderate loading, which have been tested in a full-scale test rig. The turbine's performance was mapped over a wide range of operating conditions to prove its off-design capabilities, which cover the range of operating conditions of the current research. This model is selected because the details of its geometry and performance parameters are available in the open literature, and it can be used as a benchmarking test case. In short, the turbine at its design point has a pressure ratio of 5.01, an efficiency of 92.5%, a reduced speed of $316.9 \text{ rpm}/\sqrt{K}$ and a reduced mass flow of $0.892 \text{ kg}\sqrt{K}/\text{s/kPa}$.

1D-Euler Turbine simulation tool

To evaluate the transient behavior of the turbine, a tool has been developed to solve the equations of mass, momentum, and energy conservation as the one dimensional compressible Euler equations described in Eqn. 1. The code has been initially developed for shockless explosion combustion [20] and further developed by the authors [18] for unsteady turbine simulations. The presence of turbine blades and their effect on the flow are included in the governing equations by source terms on the right side of the equations. The bleed mass flow rate that can be inserted into the turbine for cooling purposes closes the mass continuity equation. The momentum conservation equation is equipped with the blade force acting on a control volume around the blade. A schematic of a turbine rotor blade, the related control volume, and the force balance equations are shown in Fig.1. According to the second law of motion, the sum of the forces acting on the control volume can be computed as the momentum difference between the inlet and the outlet. Therefore, the blade force representing the turbine blade's presence in the momentum continuity equation is calculated (see the equations in Fig.1). The computed blade force is distributed in a concave down parabola shape from the blade inlet station to the outlet to have a more realistic

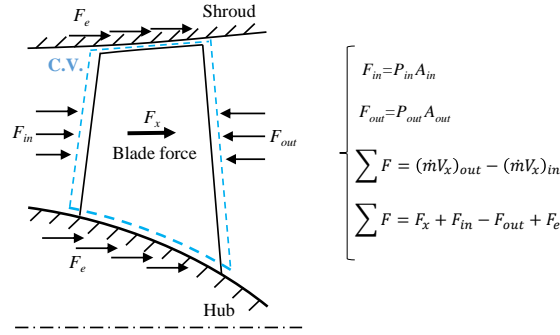


Fig. 1: A meridional view of a typical turbine rotor blade and the force balance on a control volume around the blade.

representation of the blade into the equation. If it is assumed that the blade row is adiabatic, the shaft work to close the energy continuity equation is computed by the enthalpy balance around the blade based on the first law of thermodynamics, i.e., $W = (\dot{m}h_t)_{out} - (\dot{m}h_t)_{in}$. If a bleed mass flow is injected into the turbine, the related energy terms represented by its enthalpy are added to the right side of the energy equation too.

$$\begin{aligned}
 Mass : \quad & \frac{\partial(\rho A)}{\partial t} + \frac{\partial(\rho V_x A)}{\partial x} = \frac{\partial \dot{m}_{bl}}{\partial x} \\
 Momentum : \quad & \frac{\partial(\rho V_x A)}{\partial t} + \frac{\partial(\rho V_x^2 A + PA)}{\partial x} = \frac{\partial(F_x + PA)}{\partial x} \\
 Energy : \quad & \frac{\partial(\rho EA)}{\partial t} + \frac{\partial(V_x A(\rho E + P))}{\partial x} = \frac{\partial(W + \dot{m}_{bl} h_{t,bl})}{\partial x}
 \end{aligned} \tag{1}$$

The mentioned force and work source terms are computed by a meanline analysis method. An in-house developed code has been prepared and validated against the experimental results of E³ high-pressure turbine previously [18]. The meanline program receives the turbine geometry, including the number of blades, blade inlet and outlet angles, and overall dimensions to calculate aerothermodynamic parameters between the blade rows. Since the accuracy of meanline methods depends basically on the used correlations, all the loss correlations have been fine-tuned for the test case in question based on the recommendations in open literature [21]. The source terms, which are calculated for a range of the turbine operating conditions, are provided to the 1D-Euler solver in the form of lookup tables. The solver reads the source terms from the tables based on the

blade upstream and downstream pressure magnitudes. On account of stability issues, average pressure values of five to seven neighboring cells are taken. Based on a grid size dependency analysis, each cell has a length of 0.5 mm in a domain of 470 mm length. The inlet boundary condition is computed by the PDC model that is described in the following section. Based on the experimental data, the outlet boundary condition is supplied to the solver as a constant static pressure of 3.63 bar. The constant pressure is applied since the turbine showed that it is capable of damping all the pressure fluctuations coming from the PDC configuration of this research throughout its four blade rows [18]. The details of the boundary conditions will be discussed in the course of the paper.

Pulsed Detonation Combustor Model

The 1D-Euler solver used for simulating the turbine mentioned above has been also modified to model the phenomena and the exhaust flow conditions on each PDC tube. Since the PDC tubes are assumed as straight ducts, the area term is omitted from the governing equations of Eqn.1. Also, all the mass and force source terms are set equal to zero. Considering the combustion process occurring inside the tubes, the chemical composition continuously changes in time and space. Therefore, a conservation equation for each species mass fraction is required to be solved together with the Euler equations, presented in Eqn.2. The right side of the equation represents the changes in composition resulting from chemical reactions ($\dot{Y}_{sp,chem}$) with the underlying reaction equations provided by the multi-step H₂–air mechanism described by Burke et al. [22].

$$\frac{\partial(\rho Y_{sp})}{\partial t} + \frac{\partial(\rho V_x Y_{sp})}{\partial x} = \rho \dot{Y}_{sp,chem} \quad (2)$$

Typical pulsed detonation combustion of H₂–air mixture takes place in each PDC tube, which has been explained in detail in our previous work [18]. In the current research, five tubes comprise the PDC-array configuration. Each PDC tube has a length of 1 m, and they are fired sequentially. The firing frequency of each tube is set equal to 20 Hz, resulting in a frequency for the PDC-array of 100 Hz. Following our compressor-PDC modeling [23], the PDC tubes are connected

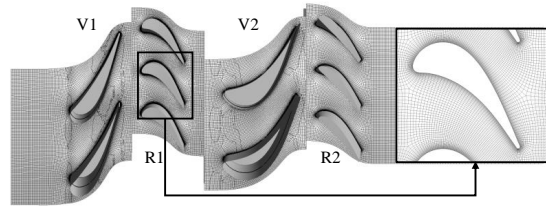


Fig. 2: An illustration of the computational domain at midspan surface.

to an upstream plenum fed by NASA-E³ compressor. The flow inside the upstream plenum is assumed to have a zero velocity, a pressure of 21.75 bar, and a temperature of 691.15 K. Once the pressure inside the tubes drops below that of the upstream plenum, air flows into the tubes. A similar plenum as at the inlet is considered at the outlet of the PDC tubes. Having the specific axial kinetic energy preserved, tube pressure is expanded to the downstream plenum pressure through an instant isentropic process. With the assumption of a zero-dimensional plenum, only mass, energy, and species fractions are considered in the conservation equations, while velocity is assumed to be always zero. The mass flow from the tubes going into the plenum is considered as mass and energy source terms within the plenum's balancing equations.

3D-CFD Method

As an expensive computational tool, the unsteady 3D-CFD analysis is utilized twice in this paper for the base turbine geometry, which is the original E³ high-pressure turbine, and the optimized geometry for the aforementioned PDC-array. The ANSYS CFX solver is employed to solve the unsteady Reynolds Averaged Navier-Stokes (RANS) equations in a three-dimensional computational domain. The domain consists of four blade rows, and the inlet and outlet planes placed one chord length upstream of the first blade row and four chord lengths downstream of the last blade row, respectively. A blade-to-blade view of the domain at midspan surface is shown in Fig.2. Since the PDC exhaust flow as the turbine inlet boundary is circumferentially symmetrical, one blade passage of each blade row has been modeled. A periodic boundary condition is assigned to the adjacent blade passages. In addition, the stage mixing plane is considered as the interface between the blade rows because fluctuations in the PDC exhaust flow are mainly in the axial direction. Therefore, the averaging in circumferential direction done in the stage mixing plane approach

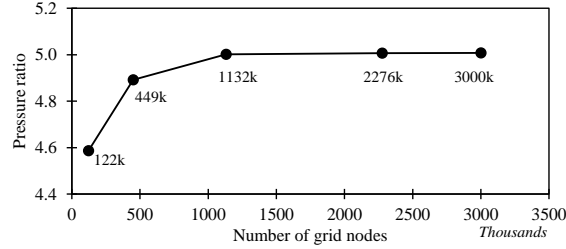


Fig. 3: Turbine pressure ratio variation with mesh size.

is applicable here. The Shear Stress Transport model developed by Menter [24] is utilized for turbulence modeling, which has been used in similar flow problems [25,26]. The approach combines the benefits of $k - \epsilon$ and $k - \omega$ models, which can model the turbulence well in near and far wall regions. The mesh discretizing the computational domain is a combination of O-H grids, depicted in Fig.2. To keep y^+ close to unity and consequently not lose the boundary layer effects, the mesh refinement is performed several times. Additionally, a mesh sensitivity study has been done with grids ranging from 122 k to 3000 k nodes. The CFD simulations have been done with these grids, and the resulting pressure ratios are compared in Fig.3. According to the results, the pressure ratio approaches the design value of 5.01 by increasing the number of grid nodes. However, more refinement from 1132 k nodes does not change the pressure ratio significantly as the relative error $((Pr_{i+1} - Pr_i)/Pr_{mean})$ becomes less than 0.1%. The Grid Convergence Index (GCI) as a metric for the mesh quality is also calculated based on the formulation by Celik et al. [27]. The GCI values corresponding to the computational domain having 1132 k grids are 0.15% and 0.2% for pressure ratio and mass flow rate, respectively, which show that further grid refinement would not have any considerable effect on the results. In the current work, a domain with 1132 k nodes is thus selected for the CFD analysis. The time step for the time-dependent simulations is a key parameter that should be specified carefully. Again, a time step dependency analysis is done for different time step sizes ranging from $20 \mu s$ to $1 \mu s$. Having an inlet boundary condition time period of 0.01 s, the mentioned time step range corresponds to 1/500 to 1/2000 of the inlet fluctuation period. Fig.4 indicates the results of three unsteady simulations with different time step sizes in terms of pressure ratio and efficiency. The comparison of the results shows that the appropriate time step is $10 \mu s$ and any further reduction leads to a negligible change in the results of the transient simulation at a

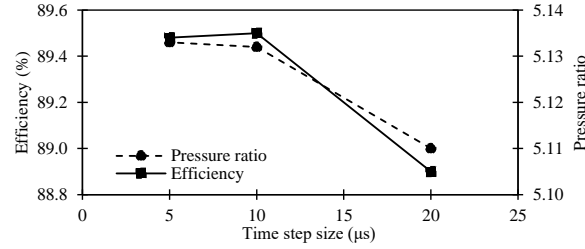


Fig. 4: Effect of time step size on performance parameters.

substantial computational cost. Each unsteady 3D-CFD simulation in this research takes around 36 computational hours to converge using a computer cluster with 64 Intel® Xeon® CPUs at 3.8 GHz.

Adaptive Surrogate Model-Based Optimization

Surrogate model-based optimization (SBO) methods effectively solve implicit, complex, and time-consuming optimization problems that need several calls to the objective function. These methods are widely used in engineering-related problems, specifically in aerospace engineering [28]. In general, an SBO includes a process of sampling, evaluating high fidelity objective functions, creating a surrogate model, and finding the optimum design. The computational cost of an optimization problem depends mainly on the number of objective function calls. Therefore, creating a surrogate model will reduce this number by quickly and intelligently selecting the optimum design points. An adaptive sampling-based surrogate model can provide a high accuracy by employing infilling strategies to use auxiliary points for modifying the surrogate model. A proper searching approach to find the sampling infill criteria would guide the solution and increase the effectiveness of the optimization procedure. An adaptive surrogate model-based optimization framework is applied in this paper, which is shown in Fig.5. The process starts by selecting initial samples from the whole design space, which includes the optimization variables. The accuracy of the surrogate model itself is a function of sample numbers, and their spatial distribution [29]. In this paper, the initial samples from the design space, which will be elaborated later, are selected by a Latin Hypercube Design (LHD). An LHD provides the samples having a suitable spatial uniformity and consequently can reflect the information of the design problem sufficiently [30]. High fidelity

objective values are found for all of these sample points. According to the type of optimization problems, the initial sample set is divided into two or more sample subsets. In this paper, there are five variables in the optimization problem in question, and the total number of initial samples is 50, which have been selected by the LHD method. The variable selection procedure will be discussed later. The subsets are selected randomly again by LHD, and five sets of 10 samples are created. Each of the subsets is used to generate a complex shape problem. For each complex shape, a surrogate model is constructed. Then the Complex Shape Method (CSM), which is a direct search algorithm, is utilized to find a proper new infill point by doing some operations of reflection, expansion, contraction, and compression expressed in Eqn.3.

$$\begin{aligned}
 &\text{Sample points : } X_i, \quad i = 1, 2, \dots, n \\
 &\text{Objective function value : } f(X_i) \\
 &f(X_w) = \text{maximum}(f(X_i)), \quad i = 1, 2, \dots, n \\
 &f(X_b) = \text{minimum}(f(X_i)), \quad i = 1, 2, \dots, n \\
 &X_s = \frac{1}{n-1} \sum_{i=1}^n X_i, \quad i \neq w \\
 &\text{Reflection : } X_{Ref} = X_s + \zeta(X_s - X_w), \quad \zeta > 1 \\
 &\text{Expansion : } X_{Exp} = X_{Ref} + \kappa(X_{Ref} - X_s), \quad \kappa > 0 \\
 &\text{Contraction : } X_{Cont} = X_s + \vartheta(X_s - X_w), \quad \vartheta < 0 \\
 &\text{Compression : } X_{i,new} = X_b - 0.5(X_b - X_i), \quad i = 1, 2, \dots, n \text{ \& } i \neq b
 \end{aligned} \tag{3}$$

X_w is the worst sample point among the current sample point subset, which corresponds to the maximum objective function value. By creating the complex shape and doing the reflection operation (with a recommended reflection factor of $\zeta = 1.3$), the new sample point is generated. If the objective function value of the new sample point is lower than the lowest function value in the current complex shape, the expansion operation is done. The expansion factor is initially selected greater than 1. Provided that the expansion operation fails to generate a better sample point, the expansion factor is reduced by a factor of 0.5 until $\kappa = 10^{-5}$. If the objective function value of the reflected sample point is greater than the worst sample point, the contraction operation is run to move away from the worst point. Presuming that none of the mentioned operations leads to an objective function value better than the worst one, $n - 1$ new sample points will be generated

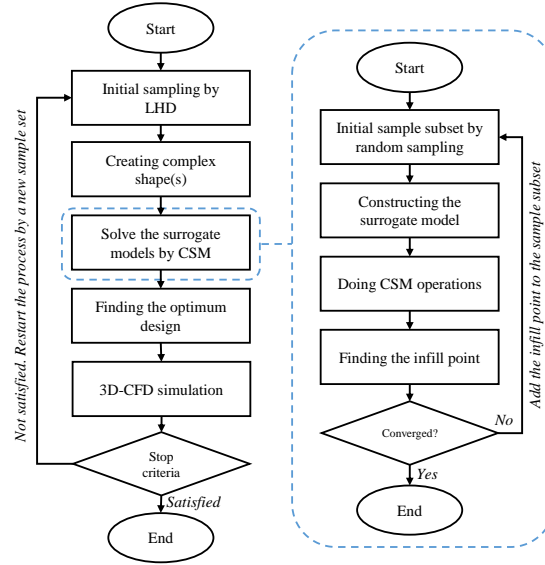


Fig. 5: The adaptive optimization framework.

using the compression operation. This operation compresses the sample points toward X_b as the best sample among the sample point subset to form a new complex shape together with it. Then the calculation starts anew. The existing criteria must be checked within all of the operations, and the sample points must be inside the range. Using these operations, the new sample point by which the worst point is replaced is constantly approaching the optimum solution while continuously improving the surrogate model's local precision.

A sample process of complex shape creation in a two-dimensional design space with three initial sample points is shown in Fig.6. In this example, the searching process uses reflection or expansion operation in each iteration to create a new complex shape and finally reaches point 8, which is the optimum solution (minimum objective function value). Dashed lines represent the operations to find the new sample points passing through the geometric center of the complex shape, excluding the worst point. For design spaces with higher dimensions and more initial sample point numbers, the complex shape is no longer presented by a triangle and becomes more intricate. The basics of CSM have been elaborated and applied for some engineering applications by Xu et al. [31]. Once the new infill point is getting close enough to the previous one and the convergence criteria, i.e., $\Delta X_{i,i+1}/(X_{max} - X_{min}) < 10^{-4}$, is satisfied, the operation ends, and the optimum design out of the complex shape is found. Otherwise, the infill sample point is substituted

for the worst sample point in the initial sample subset, and the surrogate model is updated. The Kriging method, a popular spatial interpolation model based on the Gaussian process, is utilized to construct the surrogate model. Since the Kriging method provides nonlinear functions with satisfactory approximation abilities by using a unique error estimation function, it is widely used in similar applications [32–34]. The final optimum design, which is the best optimum one out of all the complex shapes, will be simulated using a 3D-CFD analysis and compared to the original design. If the optimum design does not satisfy the expectations, the whole procedure will be restarted by a new initial sample set. Since the construction process of the surrogate model is closely merged with the optimization process, the mentioned optimization method has the advantages of having a simple modeling process, a small sample size, and high optimization efficiency. CSM combines the process of finding the infill points and the optimization process into one loop. In this method, the surrogate model is continuously updated and directed to the optimal solution. Therefore, unlike the other optimization approaches, the accuracy of the surrogate model does not need to be verified in the iterative process outside the searching process. Although the efficiency of the optimization algorithm depends on the nature of the problem, CSM proves its superior efficiency over the other approaches in benchmark function problems having multiple local minimums, e.g., the well-known test functions of Sasena, Goldstein price, three-dimensional Hartman, and six-dimensional Hartman [31]. As a direct searching algorithm, CSM uses fewer sample points, and hence fewer objective function calls than the expected improvement algorithm [35], candidate point approaches [36] and maximized response surface method [37], in solving each of the mentioned test functions. In general, if multiple extremums exist in the objective function, increasing the number of complex shapes can prevent the algorithm from getting stuck in a local optimum solution. Nevertheless, because different complex shapes may search in the same direction, too much increasing the number of complex shapes brings unnecessary sample points to the calculation and subsequently increases the computational cost and reduces the algorithm efficiency. Therefore, a fair number of complex shapes can help the search efficiency of the optimization algorithm. Depending on the optimization problem, an initial number of complex shapes should be selected. Then, based on the searching directions and the optimums found out of the complex shapes, one can decide

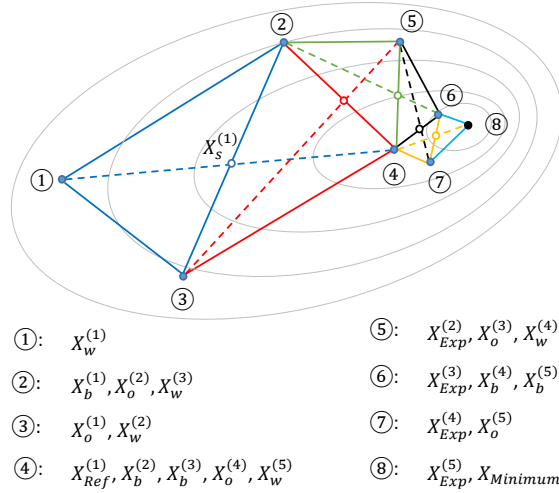


Fig. 6: A sample CSM iteration process in a two dimensional design space.

whether more complex shapes are required. If a majority of the complex shapes are converged to an optimum which is the best, it can be ensured that the algorithm has reached the global optimum.

RESULTS AND DISCUSSION

In this section, firstly, the variable selection and the objective function for the optimization purpose are explained. After that, the boundary conditions for the objective function calculations are defined. Consequently, the optimization results will be elaborated, including the convergence trend and the optimum values. Finally, the unsteady 3D-CFD simulation results for the optimum design will be compared against the original one to evaluate the process. The comparisons are made mainly in the scope of turbine performance parameters of entropy generation, total pressure loss, and turbine power.

Objective Function and Variables

The goal of the optimization process in this paper is to find an optimum turbine design having the highest efficiency while working under PDC exhaust flow. The efficiency term includes both pressure ratio and work output. In this regard, entropy generation quantifies the losses and directly affects efficiency. For this reason, it is used to visualize and identify losses in the current work.

The non-dimensional entropy, defined in Eqn.4, is used as the objective to be minimized. The temperature and pressure reference values are set to 1 K and 1 pa, respectively. Non-dimensional entropy generation is computed by subtracting the non-dimensional entropy at the turbine outlet from the inlet. It should be noted that, in the course of this paper, the entropy term refers to as non-dimensional entropy, defined in Eqn.4.

$$S = (T/T_{ref})^{\frac{\gamma}{\gamma-1}} (P/P_{ref})^{-1} \quad (4)$$

There are many parameters that can be involved in a turbine optimization process which include geometrical parameters, thermodynamic parameters, or basic turbine design parameters [21]. According to the scope of this paper and the available test case geometry, the optimization focuses on the geometrical parameters to evaluate the optimization methodology. To have the highest possible involvement of the 1D-Euler methodology as the objective function evaluation method, the focus is set on the turbine geometrical variables that affect loss. Therefore, it is assumed that the overall annulus geometry of the original turbine is fixed. Besides, previous studies [18, 25, 38] showed that almost half of the unsteadiness is damped through the first blade row, meaning that the first turbine stage experiences most of the PDC exhaust flow unsteadiness. Hence, the emphasis is put on the first stage geometrical variables. According to the loss correlations for turbine blades used in the meanline method, blade inlet and outlet metal angles, blade thickness, and solidity play significant roles in loss generation. Solidity is defined as the ratio of chord length to blade spacing. If the chord length is assumed to be fixed, the solidity will be a function of the blade number. Since the turbine inlet is connected to a plenum with the assumption of axially fluctuating flow entering the turbine, the first blade inlet metal angle could be fixed since it already has a zero incidence angle. Consequently, based on the profile loss correlation [21], the effect of the maximum thickness of the first blade row on loss generation is canceled. To decouple the relatedness of the upstream blade outlet angle from the downstream blade inlet angle, only the blade outlet angle is considered as a variable. As a result, the design space includes five optimization variables of two solidities, two blade outlet angles, and a maximum thickness to chord

Table 1: Optimization variables and their bounds.

Variable	NB_V	NB_R	β_V	β_R	$t_{r,max}/c$
Base value	46	76	16	24	0.258
Bounds	29-116	54-198	20-50	20-50	0.15-0.30

ratio.

According to the available loss correlations reported by Aungier [21], the blade solidity can vary from 0.8 to 5. If the chord lengths are assumed to be fixed, the number of blades for each blade row can vary in a space not exceeding the solidity range. According to the blade thickness, some high values of solidity can not be chosen due to the space limitation between the adjacent blades, which is a design space constraint. Blade outlet angle ranges are also provided in the loss correlation between 20 and 50 degrees. It is generally recommended that a maximum thickness to chord ratio of 0.2 is a proper choice for the turbine blades. Nevertheless, a range is assigned to the thickness to chord ratio of the rotor blade, which is from 0.15 to 0.30. The optimization variables, the original values, and the ranges are tabulated in Tab.1.

Boundary Conditions

The optimization process is done using the unsteady 1D-Euler simulation of the turbine as the objective function evaluation tool. The unsteadiness comes from the upstream boundary condition, where a five PDC tube configuration is operating. The PDC model, presented in the methods section, computes the total pressure and the total temperature at the turbine inlet. Figure 7 indicates the computed turbine inlet boundary condition. The pressure and temperature fluctuations has an relative amplitude of 9.7% and 7.2%, respectively, which is defined as $((\phi_{max} - \phi_{min})/2\phi_{mean})$. The simulation has been repeated several times by trying different distances from the last blade row to the outlet plane, and the intermediate results were checked downstream of the turbine. It was observed that the turbine could dampen all the levels of fluctuations existing in the inlet boundary condition. For this reason, the turbine outlet boundary condition is set to have a fixed static pressure of 3.63 bar. The same boundary condition is applied for the 3D-CFD simulations in

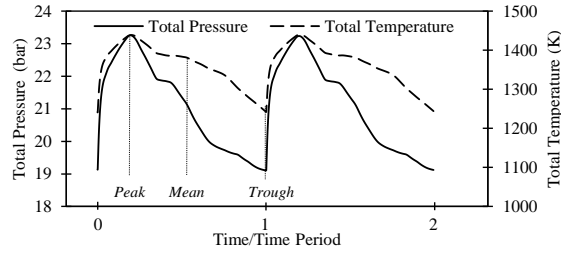


Fig. 7: Turbine inlet boundary conditions.

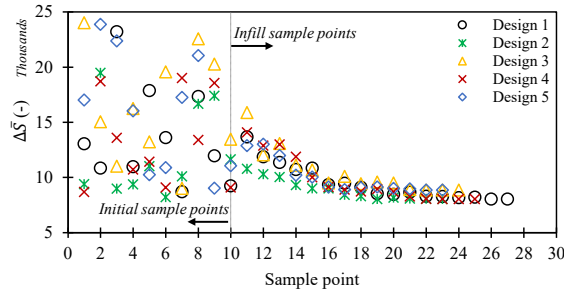


Fig. 8: Convergence trend of the optimization process.

this research.

Optimization Results

Following the optimization procedure described in the method section, the optimization is run, and five designs were generated out of the created complex shapes. Each of the complex shapes was iterated less than 20 times to reach its optimum objective function value satisfying the convergence criteria. Figure 8 depict the convergence trend for each design, starting from their randomly selected initial sample points. It is observed that three out of five designs based on complex shapes converge to the same minimum objective function of $\Delta\bar{S} = 8034$, which shows global optimum design. The optimum design parameters are listed in Tab.2 with an illustration of the related blade shape modifications in Fig.9.

The optimization procedure suggests a decrease in the number of blades from 46 to 40 which corresponds to a reduction in solidity from 1.30 to 1.13 and an 8 degree increase in blade outlet angle for nozzle blades. For rotor blades, the number of blades is increased from 76 to 84, meaning an increase in solidity from 1.26 to 1.40. As is suggested for nozzle blades, the rotor outlet angle

Table 2: Optimization results.

	$\Delta \bar{S}$	NB_V	NB_R	β_V	β_R	$t_{r,max}/c$
Base	9595	46	76	16.0	24	0.258
Optimized	8034	40	84	24.1	31.5	0.259

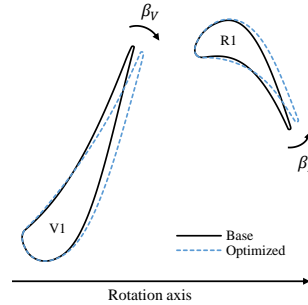


Fig. 9: Blade angle modifications at midspan surface.

is increased by 5.5 degrees. Rotor thickness to chord ratio almost remains unchanged for the optimum design. Based on these changes in the first turbine stage blade rows, the overall entropy generation, averaged over a pulse of the PDC, is reduced by 16%.

Entropy Generation

To evaluate the optimized geometry and compare the consequence of the modifications to the blades more precisely, transient 3D-CFD simulations have been performed for both base and optimized cases. Mass-averaged entropy values at inlet and outlet turbine planes have been computed once the periodic convergence has been achieved. Figure 10 illustrates the instantaneous entropy over a pulse period for the base and optimum designs. The overall trend in entropy in the outlet plane is the same as in the inlet plane with a right shift in time which is related to the flow passing time through the domain. In general, a downshift in the outlet entropy can be seen for the optimized case compared to the base design.

To better visualize how the blades reduce the entropy generation in the optimized design, the entropy contour around the first stage rows is plotted in Fig.11 at the instant of peak entropy

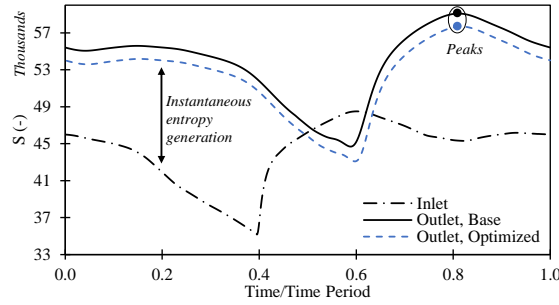


Fig. 10: Time dependent entropy at the turbine inlet and outlet.

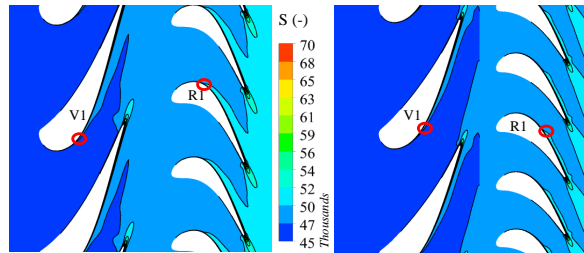


Fig. 11: Entropy contour around the first stage blades at midspan surface at the overall peak entropy generation instant, base (left) and optimized (right) designs.

at the outlet. Red circles show the start of increment in entropy on the suction surfaces of the blades. According to the circles' locations moving toward the trailing edges, both blade rows perform better in terms of entropy generation, while the share of rotor blades is more pronounced. In the optimized geometry, the divergent section of the blade passages becomes smoother so that the flow tends to be more attached and produce less entropy. A lower entropy region downstream of the rotor blades can be seen in the optimum design contour as well. The higher entropy regions on the suction surface of the blades in the base case can be explained by their greater uncovered turning angles. The lower uncovered turning downstream of the blade throat in the optimized design, which results from the blade outlet angle increment, make the flow follow the trailing edge and preserve the pressure gradient so that the boundary layer remains attached. In some cases where the uncovered turning is too large, the flow deviates from the trailing edge, affecting flow turning and the work output adversely [13,39].

Each of the blade rows has a different contribution to the overall entropy generation. Figure 12 shows the time-averaged entropy calculated at upstream and downstream planes of the blade

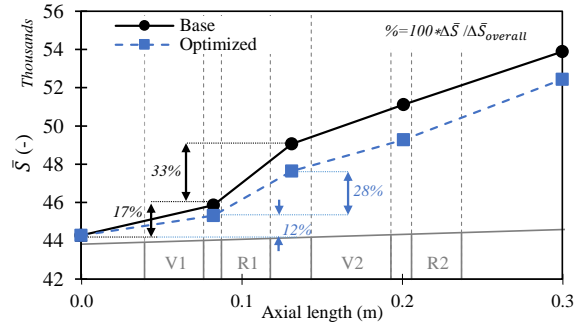


Fig. 12: Averaged entropy distribution throughout the turbine.

rows for both cases. The blade rows in the meridional view are schematically depicted inside the figure just as an axial location reference and do not represent the actual view. Comparing the entropy generation by the first stationary row in the optimum design against the base design shows a reduction from 17% to 12% of the whole amount of entropy generated in the turbine. The same comparison for the first rotor row indicates that the optimum design has 5% lower entropy generation than the base case. It can be seen that the share of entropy generation by the first stage is reduced from 50% in baseline to 40% in the optimum design. This shows the second stage has a higher entropy generation contribution than the first stage in the optimum design. Having a qualitative look at the interstage entropy results in Fig.12, the entropy difference between the two designs is increasing from the inlet up to the upstream of the last blade row. In contrast, the difference from there to the outlet plane does not follow the same trend. This discrepancy, together with the fact that in the optimized design, the share of the first stage in the overall turbine entropy generation is lower than that of the second stage (40% versus 60%), indicates that the optimization process was successful in modifying the first stage toward lowering entropy generation even to a level even lower than the second stage which is less affected by the unsteadiness.

Total Pressure Loss

Total pressure loss is a second reference parameter measuring the performance of a blade, specifically in cascade flow analysis from which loss correlations are developed. Table 3 lists the total pressure loss coefficients of the first stage rows, defined here as $\omega = \Delta P_t / P_{t,inlet}$. According to the table, it is apparent that the first stator could perform better in the optimized version and

Table 3: Total pressure loss coefficient.

	Stator 1	Rotor 1	Overall
Base	0.0336	0.0292	0.0870
Optimized	0.0241	0.0258	0.0801
Change (%)	-28.2	-11.6	-7.9

generate 28.2% lower total pressure loss. The associated total pressure loss for the first rotor blades is also reduced by 11.6%. Since the modifications to the blades affect the profile shape and the blade's solidity and the fact that no shock wave was captured during the turbine operation, the reduction of pressure loss is, to a large extent, due to the profile loss reduction. According to the general profile loss formulation by Ainley-Mathieson [40], both changes are toward lowering the pressure loss coefficient within the stator row. In contrast, the solidity increment is against lowering the profile loss within the rotor row, although the optimized rotor blade achieves an overall lower total pressure loss. The overall turbine pressure loss is reduced by 7.9% as an optimization achievement.

Turbine Power

Since the turbine blade geometries are modified in the optimized design, the new turbine performance metrics change. Although the optimization process has achieved the goal of minimizing entropy generation through the turbine, the turbine output work as an important performance parameter must be checked in parallel. Ideally, it is desired to increase or maintain the turbine work as is in the base design. The total enthalpy change, namely work per unit mass, together with the averaged entropy change for each rotor row is plotted in Fig.13 for both base and optimized designs. The values are time-averaged over a pulse which are mass-averaged on the planes upstream and downstream the rows. It is seen that the optimization process reduces the first rotor work 15.7% respecting the base design while the entropy is decreased favorably by 27.5%. This enthalpy reduction can be explained by the Euler turbine equation, i.e. $\Delta H = U \Delta V_\theta$, where U is rotational velocity at a reference radius and V_θ represents tangential flow velocity. The outlet angle

of the first rotor blades is increased in the optimized version from the base design. While the inlet angle is kept constant, the blade curvature is decreased so that the blade role in turning the incoming flow is reduced (see Fig.9). The averaged flow turning by the first rotor blade is calculated over a pulse, and the corresponding values are 92 degree and 78 degree for the base and optimized cases, respectively. Thus, less enthalpy change is anticipated in the optimized case. Contrary to the first rotor row, the second rotor row exhibits a reverse change in work extraction and entropy generation. It has 20.5% higher work per unit mass than the base design in the optimized turbine configuration. The second rotor generates higher entropy in the optimized configuration than the baseline. Since the blade geometry of the second rotor row is identical in both cases, the reason can be found in axial velocity magnitude and the first stationary vane modifications made in the optimized design. The outlet blade angle of the first vane is increased similar to the first rotor blades, and also the number of blades is decreased. While the rotational speed is fixed, these changes, together with the resulting increase in the inlet flow area of the first stationary vanes, lead to an increase in the overall mass flow rate. Since the number of the rotor blades is increased in the optimized case, a higher axial velocity inside the rotor blade passages has resulted than the base case. The time-averaged mass flow rates are 53.1 kg/s and 61.4 kg/s for base and optimized designs respectively. Therefore, according to the velocity triangle, higher work output is expected from the second rotor row. In the case of the first rotor row, the effect of change in blade turning angle on the output work is more dominant than that of the related change in axial velocity magnitude. The overall work per unit mass for the whole turbine is also calculated, showing a 1% reduction in the optimized design compared to the base case. As reported before, the overall entropy is reduced in the optimum design by 16%. To compare the output turbine power, the time-dependent power over a pulse is depicted in Fig.14. While the overall trends of the instantaneous power are identical for both designs, the optimized case produces more power over the entire pulse. The highest power is achieved at around 0.6 of time period where the entropy is the lowest (see Fig.10). The higher power is mainly due to the higher mass flow rate in the optimized design than its counterpart. The time-averaged power is 24.7 MW and 28.2 MW for the base and optimized cases, respectively. This difference indicates a 14.2% higher power that obtained by the

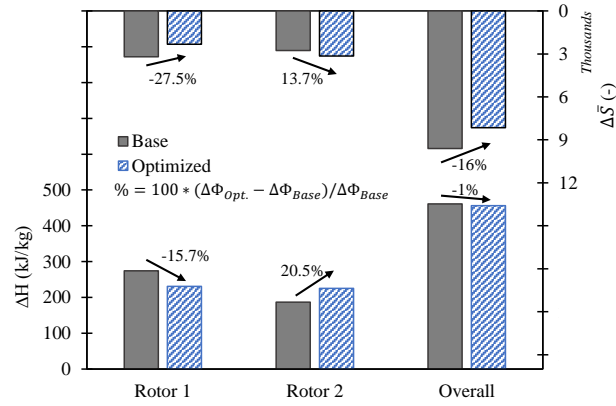


Fig. 13: Total enthalpy and entropy change in rotors.

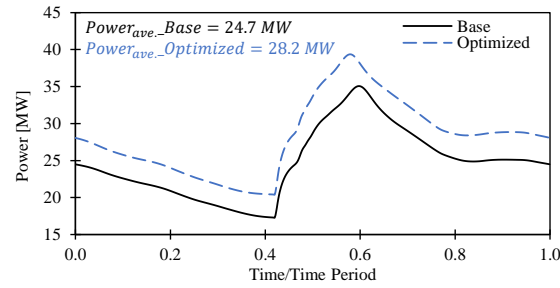


Fig. 14: Instantaneous turbine output power.

optimization process.

Steady-State operation

To evaluate how the optimized geometry performs in steady-state conditions, the inlet pulse is divided into three discrete points of trough, mean and peak of the pulse (see Fig.7). Steady 3D-CFD simulations are performed by applying each of these conditions as the inlet boundary. The mass-averaged entropy generation for the first stage is calculated and depicted in Fig.15. The results show that the optimized stage, which is optimized based on the unsteady operation over the entire inlet pulse, has a lower entropy generation in steady operations as well. The differences between the entropy generation by the two geometries, displayed with a dash-dot curve in Fig.15, are 20.2%, 21.3%, and 22% at trough, mean, and peak points, respectively. Although the optimized stage has a little better performance at the peak point than at the other points, it is concluded that the optimization process brings a geometry that can work almost the

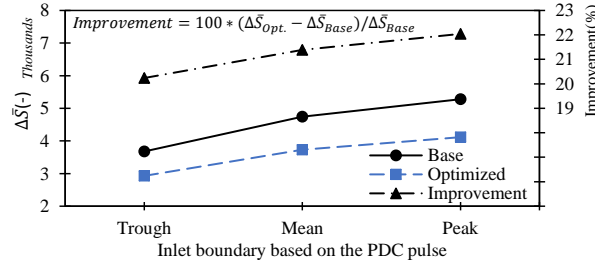


Fig. 15: Entropy generation of the first stage in steady-state operation at the inlet boundaries equal to trough, mean, and peak of the PDC pulse.

same under different steady-state conditions over a pulse. In contrast, an optimization based on the steady operations at trough and peak points by Fernelius et al. [13] for an unsteady turbine, working under a sinusoidal boundary condition, showed that the entropy generation improvement by the geometries optimized at these points can be very different (a difference around 50%).

CONCLUSION

In this paper, a fast approach for a PDC-operated turbine performance optimization is presented and evaluated. A method has been introduced to evaluate the objective function as the main part of the optimization, which integrates an unsteady 1D-Euler turbine simulation, a mean-line steady-state analysis, and a PDC numerical model. The latter two provide the 1D-Euler simulation with the turbomachinery source terms and the time-dependent PDC boundary conditions, respectively. The optimization was performed using an adaptive surrogate model-based framework that utilizes the complex shape method as a searching algorithm. The approach was run for a two-stage turbine to minimize the entropy generation by modifying some geometrical parameters in the first stage, which experiences the highest unsteadiness from PDC exhaust flow. The optimized design was compared to the base design using the unsteady 3D-CFD simulations to evaluate the accuracy of the optimization approach and validate the new design.

The optimization results showed that the new design has a lower solidity in the first stationary vanes but higher in rotor blades than the base case. The blade outlet angles were recommended to open slightly so that the blade turnings were reduced while the maximum thickness to chord ratio of the first rotor blades was almost unchanged. The optimum design showed a 16% reduction in

entropy generation and a 14.2% gain in the overall turbine power. The unsteady 3D-CFD results indicated that the lower entropy generation is due to the shortening of the flow wake region on the suction surface of the blades in the optimized geometries, and the higher output power is mainly because of the higher mass flow rate in the new design. Additionally, the rotor blades showed a more noticeable role in lowering the entropy generation than the stationary vanes.

All in all, the optimization methodology, coupled with a fast unsteady turbine simulation tool, was proven to be effective in unsteady turbine optimization problems. The main advantage of the proposed algorithm lies in the objective function evaluation procedure that considers unsteadiness within the optimization loops. Although the unsteady effects in turbomachinery make any 3D-CFD method highly expensive and almost impossible to be integrated into the related optimization problems, the proposed approach showed its robustness and applicability. Therefore, the methodology enables the designers to perform optimizations over a wide range of variables within a reasonable time. It should be noted that since it is the meanline analysis that provides the source terms to the unsteady 1D-Euler simulation tool, considering the nature of this method, there might be a limitation in selecting the optimization variables. Suppose the desired optimization variables cannot be included directly in the meanline analysis, e.g., specific modifications to the blade profile or any hub or shroud contouring, for which there is no correlation available. In that case, one can replace the meanline method with the steady-state CFD simulation, which does not impose much computational cost.

ACKNOWLEDGEMENTS

The authors would like to acknowledge the financial support from Elsa Neumann Foundation (NaFöG). Additionally, Norddeutscher Verbund für Hoch- und Höchstleistungsrechnen (HLRN) is acknowledged for providing the high performance computing resources.

REFERENCES

- [1] International Energy Agency, 2021. "Global Energy Review 2021". *Global Energy Review 2020*, pp. 1–36.

- [2] Stathopoulos, P., 2018. "Comprehensive Thermodynamic Analysis of the Humphrey Cycle for Gas Turbines with Pressure". *Energies*, **11**(3521).
- [3] Paxson, D. E., and Kaemming, T. A., 2012. "Foundational performance analyses of pressure gain combustion thermodynamic benefits for gas turbines". *50th AIAA Aerospace Sciences Meeting Including the New Horizons Forum and Aerospace Exposition*(January), pp. 1–13.
- [4] Stathopoulos, P., Rähse, T., Vinkeloe, J., and Djordjevic, N., 2020. "First law thermodynamic analysis of the recuperated humphrey cycle for gas turbines with pressure gain combustion". *Energy*, **200**, 6, p. 117492.
- [5] Glaser, A., Caldwell, N., and Gutmark, E., 2007. "Performance of an Axial Flow Turbine Driven by Multiple Pulse Detonation Combustors". *45th AIAA Aerospace Sciences Meeting and Exhibit*(January), pp. 1–10.
- [6] Rasheed, A., Furman, A., and Dean, A., 2005. "Experimental Investigations of an Axial Turbine Driven by a Multi-Tube Pulsed Detonation Combustor System". In *41st AIAA/ASME/SAE/ASEE Joint Propulsion Conference & Exhibit*, no. July, American Institute of Aeronautics and Astronautics, pp. 1–13.
- [7] Rasheed, A., Furman, A. H., and Dean, A. J., 2011. "Experimental Investigations of the Performance of a Multitube Pulse Detonation Turbine System". *Journal of Propulsion and Power*, **27**(3), pp. 586–596.
- [8] Anand, V., St. George, A., Knight, E., and Gutmark, E., 2019. "Investigation of pulse detonation combustors — Axial turbine system". *Aerospace Science and Technology*, **93**, 10, p. 105350.
- [9] Fernelius, M. H., and Gorrell, S. E., 2020. "Mapping Efficiency of a Pulsing Flow-Driven Turbine". *Journal of Fluids Engineering*, **142**(6), 6, pp. 1–8.
- [10] Van Zante, D., Envia, E., and Turner, M. G., 2007. "The Attenuation of a Detonation Wave By an Aircraft Engine Axial Turbine". In *ISABE*, no. September, pp. 1–12.
- [11] Xisto, C., Petit, O., Grönstedt, T., Rolt, A., Lundbladh, A., and Paniagua, G., 2018. "The efficiency of a pulsed detonation combustor–axial turbine integration". *Aerospace Science and Technology*, **82-83**(August), 11, pp. 80–91.

- [12] Cuciumita, C., and Paschereit, C. O., 2019. "Numerical Performance Assessment of a Turbine Blade Row Operating Under Pulsed Detonation Combustion Inlet Conditions". In Volume 2B: Turbomachinery, American Society of Mechanical Engineers.
- [13] Fernelius, M. H., and Gorrell, S. E., 2021. "Design of a Pulsing Flow Driven Turbine". *Journal of Fluids Engineering, Transactions of the ASME*, **143**(4), pp. 1–9.
- [14] Yang, M., Deng, K., Martines-Botas, R., and Zhuge, W., 2016. "An investigation on unsteadiness of a mixed-flow turbine under pulsating conditions". *Energy Conversion and Management*, **110**, pp. 51–58.
- [15] Taddei, S. R., 2020. "Time-marching solution of transonic flows at axial turbomachinery meanline". *Proceedings of the Institution of Mechanical Engineers, Part G: Journal of Aerospace Engineering*, 12, p. 095441002097735.
- [16] Dittmar, L., and Stathopoulos, P., 2020. "Numerical Analysis of the Stability and Operation of an Axial Compressor Connected to an Array of Pulsed Detonation Combustors". In Volume 5: Controls, Diagnostics, and Instrumentation; Cycle Innovations; Cycle Innovations: Energy Storage, American Society of Mechanical Engineers.
- [17] Chiong, M. S., Rajoo, S., Romagnoli, A., Costall, A. W., and Martinez-Botas, R. F., 2014. "Integration of meanline and one-dimensional methods for prediction of pulsating performance of a turbocharger turbine". *Energy Conversion and Management*, **81**, pp. 270–281.
- [18] Asli, M., Garan, N., Neumann, N., and Stathopoulos, P., 2021. "A robust one-dimensional approach for the performance evaluation of turbines driven by pulsed detonation combustion". *Energy Conversion and Management*, **248**, 11, p. 114784.
- [19] Timko, L. P., 1984. Energy Efficient Engine High Pressure Turbine Component Test Performance Report. Tech. rep., General Electric Co. Cincinnati, OH, United States.
- [20] Berndt, P., Klein, R., and Paschereit, C. O., 2016. "A kinetics model for the shockless explosion combustion". *Proceedings of the ASME Turbo Expo*, **4B-2016**, pp. 1–8.
- [21] Aungier, R. H., 2006. *Turbine Aerodynamics: Axial-Flow and Radial-Flow Turbine Design and Analysis*. ASME Press, Three Park Avenue New York, NY 10016-5990, 1.
- [22] Burke, M. P., Chaos, M., Ju, Y., Dryer, F. L., and Klippenstein, S. J., 2012. "Comprehensive

- H₂/O₂ kinetic model for high-pressure combustion”. *International Journal of Chemical Kinetics*, **44**(7), 7, pp. 444–474.
- [23] Neumann, N., Asli, M., Garan, N., Peitsch, D., and Stathopoulos, P., 2021. “A fast approach for unsteady compressor performance simulation under boundary condition caused by pressure gain combustion”. *Applied Thermal Engineering*, 6, p. 117223.
- [24] Menter, F. R., 1994. “Two-equation eddy-viscosity turbulence models for engineering applications”. *AIAA Journal*.
- [25] Asli, M., Stathopoulos, P., and Paschereit, C. O., 2021. “Aerodynamic Investigation of Guide Vane Configurations Downstream a Rotating Detonation Combustor”. *Journal of Engineering for Gas Turbines and Power*, **143**(6), 6.
- [26] Sousa, J., Paniagua, G., and Saavedra, J., 2017. “Aerodynamic response of internal passages to pulsating inlet supersonic conditions”. *Computers and Fluids*, **149**, pp. 31–40.
- [27] Celik, I. B., Ghia, U., Roache, P. J., Freitas, C. J., Coleman, H., and Raad, P. E., 2008. “Procedure for Estimation and Reporting of Uncertainty Due to Discretization in CFD Applications”. *Journal of Fluids Engineering*, **130**(7), p. 078001.
- [28] Yondo, R., Andrés, E., and Valero, E., 2018. “A review on design of experiments and surrogate models in aircraft real-time and many-query aerodynamic analyses”. *Progress in Aerospace Sciences*, **96**(March), 1, pp. 23–61.
- [29] Jin, Y., 2005. “A comprehensive survey of fitness approximation in evolutionary computation”. *Soft Computing*.
- [30] Montgomery, D. C., 2017. *Montgomery: Design and Analysis of Experiments*.
- [31] Xu, H., Liu, L., and Zhang, M., 2020. “Adaptive surrogate model-based optimization framework applied to battery pack design”. *Materials & Design*, **195**, 10, p. 108938.
- [32] Han, Z.-H., Zhang, Y., Song, C.-X., and Zhang, K.-S., 2017. “Weighted Gradient-Enhanced Kriging for High-Dimensional Surrogate Modeling and Design Optimization”. *AIAA Journal*, **55**(12), 12, pp. 4330–4346.
- [33] Baert, L., Chérière, E., Sainvitu, C., Lepot, I., Nouvellon, A., and Leonardon, V., 2020. “Aerodynamic Optimization of the Low-Pressure Turbine Module: Exploiting Surrogate Models in a

- High-Dimensional Design Space”. *Journal of Turbomachinery*, **142**(3), 3, pp. 1–11.
- [34] Gao, H. F., Zio, E., Wang, A., Bai, G. C., and Fei, C. W., 2020. “Probabilistic-based combined high and low cycle fatigue assessment for turbine blades using a substructure-based kriging surrogate model”. *Aerospace Science and Technology*.
- [35] Jones, D. R., Schonlau, M., and Welch, W. J., 1998. “Efficient Global Optimization of Expensive Black-Box Functions”. *Journal of Global Optimization*, **13**(4), pp. 455–492.
- [36] Regis, R. G., and Shoemaker, C. A., 2007. “A stochastic radial basis function method for the global optimization of expensive functions”. *INFORMS Journal on Computing*.
- [37] Regis, R. G., and Shoemaker, C. A., 2013. “A quasi-multistart framework for global optimization of expensive functions using response surface models”. In *Journal of Global Optimization*.
- [38] Bakhtiari, F., and Schiffer, H.-P., 2019. “Numerical approach to the modelling of transient interaction of prospective combustor concepts and conventional high pressure turbines”. *Propulsion and Power Research*, **8**(1), 3, pp. 1–12.
- [39] Coull, J. D., 2017. “Endwall loss in turbine cascades”. *Journal of Turbomachinery*, **139**(8), pp. 1–12.
- [40] Ainley, D. G., and Mathieson, C. R., 1951. A Method of Performance Estimation for Axial-Flow Turbines. Tech. Rep. 2974.

LIST OF FIGURES

1	A meridional view of a typical turbine rotor blade and the force balance on a control volume around the blade.	8
2	An illustration of the computational domain at midspan surface.	10
3	Turbine pressure ratio variation with mesh size.	11
4	Effect of time step size on performance parameters.	12
5	The adaptive optimization framework.	14
6	A sample CSM iteration process in a two dimensional design space.	16
7	Turbine inlet boundary conditions.	19
8	Convergence trend of the optimization process.	19
9	Blade angle modifications at midspan surface.	20
10	Time dependent entropy at the turbine inlet and outlet.	21
11	Entropy contour around the first stage blades at midspan surface at the overall peak entropy generation instant, base (left) and optimized (right) designs.	21
12	Averaged entropy distribution throughout the turbine.	22
13	Total enthalpy and entropy change in rotors.	25
14	Instantaneous turbine output power.	25
15	Entropy generation of the first stage in steady-state operation at the inlet boundaries equal to trough, mean, and peak of the PDC pulse.	26

LIST OF TABLES

1 Optimization variables and their bounds. 18

2 Optimization results. 20

3 Total pressure loss coefficient. 23